Soft Matter

PAPER

View Article Online
View Journal | View Issue

Cite this: *Soft Matter*, 2018, **14**, 8771

Mechanics of biomimetic 4D printed structures†

Wim M. van Rees, ‡*[ab] Elisabetta A. Matsumoto, [ac] A. Sydney Gladman,[ad] Jennifer A. Lewis[ae] and L. Mahadevan *[aef]

Received 14th May 2018,
Accepted 10th October 2018

DOI: 10.1039/c8sm00990b

rsc.li/soft-matter-journal

Recent progress in additive manufacturing and materials engineering has led to a surge of interest in shape-changing plate and shell-like structures. Such structures are typically printed in a planar configuration and, when exposed to an ambient stimulus such as heat or humidity, swell into a desired three-dimensional geometry. Viewed through the lens of differential geometry and elasticity, the application of the physical stimulus can be understood as a local change in the metric of a two dimensional surface embedded in three dimensions. To relieve the resulting elastic frustration, the structure will generally bend and buckle out-of-plane. Here, we propose a numerical approach to convert the discrete geometry of filament bilayers, associated with print paths of inks with given material properties, into continuous plates with inhomogeneous growth patterns and thicknesses. When subject to prescribed growth anisotropies, we can then follow the evolution of the shapes into their final form. We show that our results provide a good correspondence between experiments and simulations, and lead to a framework for the prediction and design of shape-changing structures.

1 Introduction

Shape-shifting objects consist of materials that undergo local expansion or compression when subjected to an environmental stimulus, such as heat, humidity, light, or a magnetic field.[1–3] Such materials are often patterned into structures using additive manufacturing methods, that then are deployed in time, resulting in the term '4D printing'.[4,5] Recent developments have made possible the routine production of such printed structures using commercially available materials and printers increasing the range of potential applications of shape-changing structures using both passive and active actuation. In the former, the material response is driven by changes in the ambient conditions, as in drug delivery,[6] whereas the latter is actively actuated, often using localized stimuli, as in robotics.[7,8]

A subclass of such shape-shifting structures are very thin and initially flat. These shape-changing plates experience mostly in-plane strain when the stimulus is applied, resulting in elastic frustration and out-of-plane buckling into a complex three-dimensional geometry.[9–11] We can distinguish between monolayer and bilayer plates: for the former, the middle surface dissects the structure into two identical halves, so that each part has the same thickness, material properties, and in-plane growth characteristics. A bilayer, instead, consists of two layers that are connected at the mid-surface, and each layer can have its own thickness, material properties, and/or growth profile. For both monolayers and bilayers, the layers can be further categorised using the type of in-plane growth assigned to their material elements. The most general type of growth is orthotropic growth, which is characterised by three degrees of freedom at each point along the layer: the two principal growth factors, and the in-plane angle of the principal axes with respect to some fixed coordinate system. Any admissible type of growth can be represented in terms of these components: for example, isotropic growth has two identical principal growth factors, and can thus be represented by one degree of freedom per point in the layer.

Within this conceptual framework of shape-changing thin structures, significant theoretical challenges need to be addressed to fully exploit the experimental capabilities. A first question is the following: given an initial shape and growth field, can we predict what form the structure takes after exposure to the stimulus?

[a] *John A. Paulson School of Engineering and Applied Sciences, Harvard University, 29 Oxford Street, Cambridge, Massachusetts 02138, USA. E-mail: lmahadev@g.harvard.edu*
[b] *Department of Mechanical Engineering, Massachusetts Institute of Technology, 77 Massachusetts Avenue, Cambridge, Massachusetts 02139, USA. E-mail: wvanrees@mit.edu*
[c] *School of Physics, Georgia Institute of Technology, 837 State Street, Atlanta, Georgia 30332, USA*
[d] *Exponent, Inc., 9 Strathmore Road, Natick, Massachusetts 01760, USA*
[e] *Wyss Institute for Biologically Inspired Engineering, Harvard University, 60 Oxford Street, Cambridge, Massachusetts 02138, USA*
[f] *Departments of Physics and Organismic and Evolutionary Biology, and Kavli Institute for NanoBio Science and Technology, Harvard University, 29 Oxford Street, Cambridge, Massachusetts 02138, USA*

† Electronic supplementary information (ESI) available. See DOI: 10.1039/c8sm00990b

‡ Present address: Department of Mechanical Engineering, Massachusetts Institute of Technology, USA.

The second question is this: how should we design the initial structure and its growth characteristics so that the final shape is closest, with respect to a specified norm, to a specific target shape?[12] More formally, these questions deal with the forward and inverse problems, respectively, of growing thin elastic structures.

Here, we focus on the forward problem, through the development and application of a numerical simulation tool to predict the shape of any thin grown structure. Our approach is based on solving the geometrically non-linear equations of elasticity for thin structures, resulting in a simple, robust and accurate tool to treat arbitrary heterogeneously growing structures with non-uniform thickness and material properties. We formulate this problem through the lens of (discrete) differential geometry, thereby naturally dealing with large displacements, growth, and the appropriate geometric invariances. This perspective enables us to solve for the equilibrium shape of heterogeneous mono- and bilayer structures with generic reference configurations and arbitrary growth patterns. The physical realization of the stimulus that causes the growth is irrelevant in this formulation of the problem, as long as the growth can be expressed using local changes in each layer's intrinsic geometry.

To demonstrate the predictive capabilities of this technique, we focus on reproducing the experimental 4D printing results described in Gladman *et al.*,[11] wherein shape-shifting structures were manufactured as a bilayer of printed filaments. Each printed filament consists of a biomimetic hydrogel-based swelling gel, locally reinforced with fibrils aligned tangentially to the filament. When immersed in water, the directional stiffening of the fibrils leads to much smaller swelling strains along the tangential direction compared with the transverse and thickness directions.

To accurately simulate the final, swollen shapes of the experimental filament-based bilayer structures, we present an algorithm to interpret such filament designs as elastic plates. The spatially varying filament density of each layer is interpreted as a non-uniform plate thickness. The filament direction and transverse and parallel growth factors of the material are used to completely determine the intrinsic geometry of each layer at each point on the mid-surface. This allows for a smooth variation of the three orthotropic degrees of freedom at every layer's location that we embed in a computational framework to capture the qualitative features of the experimentally obtained shapes.

In Section 2, we discuss the theoretical framework for the elasticity of growing mono- and bilayers, along with the details of the numerical implementation. In Section 3, we describe our approach to convert the print path design to a smoothly varying thickness field and a growth metric tensor associated with an equivalent continuous growing plate with a spatially varying thickness and growth metric. In Section 4, we show the results of our simulations and compare the results with the experimental results in Gladman *et al.*,[11] and conclude in Section 5 by discussing some future opportunities that can be addressed with this approach.

2 Variational formulation, discretisation and implementation

We start with the physical description of the printed structures in terms of the energy governing the geometric non-linear elasticity of thin monolayer and bilayers. For this, we adopt the perspective of non-Euclidean elasticity, where the strain-free reference configuration of the structure does not necessarily correspond to an admissible embedding in three-dimensional space. The theory of such plates has been subject to extensive mathematical and physical analysis,[9,13–18] and we refer to those works for further background on the topic. We then discuss the numerical discretisation of this energy and its gradient, which we use to compute minimal-energy states of the system given a certain growth profile. Finally, we provide details on the computational implementation of the discrete equations.

2.1 Elastic energy for a monolayer

The midsurface of the structure is parametrised using curvilinear coordinates $(x,y) \in U$, a closed compact subset of the Euclidean plane. This parametrisation allows us to define any embedding of the structure in space using a map $\vec{m}\colon U \to \mathbb{R}^3$. Each point $\vec{m}(x,y)$ on the embedded midsurface is characterised by its tangent vectors $\partial\vec{m}/\partial x$ and $\partial\vec{m}/\partial y$, and a unit normal vector $\vec{n} = (\partial\vec{m}/\partial x \times \partial\vec{m}/\partial y)/\|\partial\vec{m}/\partial x \times \partial\vec{m}/\partial y\|$. With this notation we can define mid-surface geometry using its first and second fundamental form, which are given as $\mathbf{a}_c = (\mathrm{d}\vec{m})^T\mathrm{d}\vec{m}$ and $\mathbf{b}_c = -(\mathrm{d}\vec{m})^T\mathrm{d}\vec{n} = -(\mathrm{d}\vec{n})^T\mathrm{d}\vec{m}$, respectively.[19]

We assume that the structure is endowed with a rest metric $\mathbf{a}_r$ and a rest second fundamental form $\mathbf{b}_r$, which represent the stress-free state of the mid-surface. From a mechanical perspective, we adopt the Kirchhoff–Love assumption that when the plate deforms, normals to the cross-section remain normal, which allows us to discard terms of $\mathcal{O}(h^4)$ and higher in the elastic energy. This further implies that the deviation of the pull-back of the metric is close to unity, *i.e.* $\|\mathbf{a}_r{}^{-1}\mathbf{a}_c - \mathbf{I}\| \leq h$, with h the thickness, consistent with the behaviour of thin structures that bend more readily than they stretch. We can then write the energy function of a monolayer with prescribed reference state $\mathbf{a}_r$ and $\mathbf{b}_r$, as[12,16,20]

$$E_{\mathrm{ML}} = \frac{1}{2}\int_U \left[\frac{h}{4}\left\|\mathbf{a}_r{}^{-1}\mathbf{a}_c - \mathbf{I}\right\|_e^2 + \frac{h^3}{12}\left\|\mathbf{a}_r{}^{-1}(\mathbf{b}_c - \mathbf{b}_r)\right\|_e^2\right]\sqrt{\det\,\mathbf{a}_r}\,\mathrm{d}x\,\mathrm{d}y, \tag{1}$$

Here $h(x,y)$ is the thickness field, and $\|\mathbf{A}\|_e^2 = \alpha\,\mathrm{Tr}^2(\mathbf{A}) + 2\beta\,\mathrm{Tr}(\mathbf{A}^2)$ defines the Saint-Venant Kirchhoff hyperelastic constitutive law used commonly in plate theory, with $\alpha = Y\nu/(1-\nu^2)$ and $\beta = Y/(2+2\nu)$, where Y is the Young's modulus and ν the Poisson's ratio of the material. For a monolayer plate, we have no initial curvature and hence set $\mathbf{b}_r = \mathbf{0}$.

Eqn (1) defines the energy of a general thin structure with rest metric $\mathbf{a}_r$ and rest second fundamental form $\mathbf{b}_r$, for any $\mathbf{a}_c$ and $\mathbf{b}_c$ determined by a specific embedding of the mid-surface. Minimising this energy over all possible embeddings yields the

equilibrium configurations of the plate, which may not be unique.

To appreciate the possible non-Euclidean character of the rest configuration, we give an example of a monolayer where initially $\mathbf{a}_r = \mathbf{I}$ and $\mathbf{b}_r = \mathbf{0}$. In this case, the minimum energy embedding of the plate's mid-surface corresponds to $\mathbf{a}_c = \mathbf{a}_r = \mathbf{I}$ and $\mathbf{b}_c = \mathbf{b}_r = \mathbf{0}$—a flat plate for which $E_{ML} = 0$. If this plate experiences isotropic growth with non-uniform scaling factor $s(x,y)$ defined at any point on the mid-surface, the metric of the grown plate becomes $\mathbf{a}_r = s(x,y)\mathbf{I}$. This change in metric causes an incompatibility, since Gauss' Theorema Egregium will generally attribute an intrinsically non-zero Gauss curvature to the surface with metric $\mathbf{a}_r$,[19] which is inconsistent with all embeddings for which $\mathbf{b}_r = \mathbf{0}$. Therefore the plate is forced to adopt an equilibrium configuration that minimises the elastic residual energy associated with $\mathbf{a}_c \neq \mathbf{a}_r$, and $\mathbf{b}_c \neq \mathbf{b}_r$. For thin structures, the bending term of $\mathcal{O}(h^3)$ implies it is energetically cheaper to relieve metric frustration through a non-zero $\mathbf{b}_c$, and so generally a buckled configuration results.

2.2 Elastic energy for a bilayer

The energy in eqn (1) corresponds to a monolayer, but this formulation can readily be extended to a bilayer of two thin plates 'glued' together at a common midsurface, equivalent to classical laminated plate theory (CLPT).[21] In this case, as discussed before, each layer will have its own growth pattern so that we can distinguish between $\mathbf{a}_{r1}$ and $\mathbf{a}_{r2}$, which are the rest metrics of the bottom and top layer, respectively. In a recent paper,[12] it was shown that substituting

$$\mathbf{a}_r = \frac{1}{2}(\mathbf{a}_{r1} + \mathbf{a}_{r2}) \quad \mathbf{b}_r = \frac{3}{4h}(\mathbf{a}_{r1} - \mathbf{a}_{r2}) \tag{2}$$

into eqn (1) provides an elastically equivalent energy of a bilayer plate with mid-surface embedding $\mathbf{a}_c$ and $\mathbf{b}_c$, rest metrics $\mathbf{a}_{r1}$ and $\mathbf{a}_{r2}$, and layer thicknesses $h/2$. The extension to non-equal layer thicknesses $h_1/2$ and $h_2/2$ can be treated similarly.[12] This energy equivalence therefore provides an easy way to implement the elastic behaviour of bilayer plates using the same implementation as used for monolayer shells.

2.3 Discretisation

With the expressions for the continuum elastic energy in place, we now proceed to discretise (1) using ideas from discrete differential geometry,[12,20,22] as summarized in Fig. 1. First, we discretise the mid-surface of our plate using a triangular mesh. For each triangle, we can then compute the local metric $(\mathbf{a}_c)_T$ from the edge vectors of that triangle in its embedding. The second fundamental form $(\mathbf{b}_c)_T$ is computed by assigning edge-normal vectors on the mid-point of each edge in the mesh and differentiating those normal vectors between the edges of a given triangle to obtain an expression for $(\mathrm{d}\vec{n})_T$ for that triangle. The edge-normal vectors are of unit length and are constrained to the edge-normal plane, so they can be represented by a single scalar angle for each edge.[20,22] Using these definitions, we can compute the first and second fundamental form of any triangle in the mesh, and given that triangle's reference fundamental

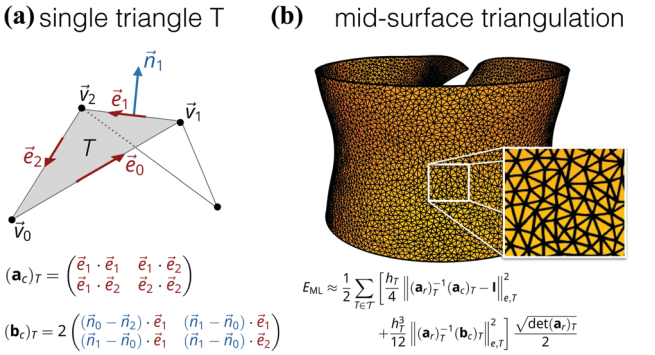

Fig. 1 (a) The discretisation of the first and second fundamental forms of a single triangle T, highlighted in grey, as a function of vertices $\mathbf{v}_i$, edges $\mathbf{e}_i$, and edge-normal vectors $\mathbf{n}_i$. (b) The triangle discretisation of the mid-surface corresponding to a catenoid (see details in Results section below) – the energy of this deformation is determined by summing the energy density over all the triangles in the mesh.

forms $(\mathbf{a}_r)_T$ and $(\mathbf{b}_r)_T$, we can compute the corresponding discrete elastic energy. Summing over all triangles provides the total energy of the deformation, so that the discretisation of eqn (1) becomes

$$E_{ML} \approx \frac{1}{2}\sum_{T\in\mathcal{T}} \left[\begin{array}{l} \frac{h_T}{4}\left\|(\mathbf{a}_r)_T^{-1}(\mathbf{a}_c)_T - \mathbf{I}\right\|_{e,T}^2 \\ +\frac{h_T^3}{12}\left\|(\mathbf{a}_r)_T^{-1}\left[(\mathbf{b}_c)_T - (\mathbf{b}_r)_T\right]\right\|_{e,T}^2 \end{array}\right]\frac{\sqrt{\det(\mathbf{a}_r)_T}}{2}. \tag{3}$$

Here the thickness per triangle is denoted by h_T and the norm $\|\cdot\|_{e,T}^2$ is defined as before as

$$\|\cdot\|_{e,T}^2 = \frac{Y_T\nu_T}{1-\nu_T^2}\mathrm{Tr}^2(\cdot) + \frac{Y_T}{1+\nu_T}\mathrm{Tr}(\cdot^2),$$

allowing for variation of all material properties per triangle. For a bilayer, we adopt the generalized form of eqn (2) for each triangle to express its discrete reference fundamental forms in terms of its prescribed discrete reference layer metrics.

The above allows us to write the embedding of the mid-surface in terms of the three-dimensional position of all vertices in the triangulation, together with the angles of all edge-normals within their respective edge-orthogonal planes. To find the equilibrium mid-surface embedding, we minimise the total elastic energy for given reference fundamental forms using the quasi-Newton minimisation algorithm L-BFGS.[23] The gradients of the energy with respect to all degrees of freedom in the mesh (the vertex positions and edge normal angles) are computed algebraically using standard results[24] and embedded in the software.

2.4 Implementation

The discretised equations are implemented using the programming language C++. Our data structures are defined in Eigen,[25] we use the libigl library[26] for general operations on triangle meshes, and shared-memory parallel processing is achieved with the Intel Threading Building Blocks (TBB) library.[27] To triangulate the mid-surfaces, we use the TRIANGLE library.[28]

2.5 Validation and example

We validated our codes using both known analytic results as well as non-linear engineering benchmarks. An example of a specific validation pertaining to this work is shown in the ESI† and corresponds to a monolayer plate, experiencing in-plane growth according to the metric of a hemisphere, and compared to a semi-analytic solution.[16]

Other examples of elementary growth patterns applied to a monolayer disk are shown in Fig. 2: a thin disk with homogeneous radial growth adopts a conical shape, and a disk with homogeneous azimuthal growth adopts a saddle shape. Intuitively, these results correspond to out-of-plane buckled shapes whose geometry accommodates the excess material in each of the respective growth directions.[29]

3 Converting the discrete print paths to a smoothed continuum description

The framework above allows us to compute equilibrium shapes given the initial shape of the plate, the material parameters and the first and second fundamental forms associated with the growth tensors. To convert this approach to predict the final shape of discrete filamentous bilayer structures as generated by the phytomimetic printing procedure, it is necessary to convert the print path design to a thickness and growth field on a continuous elastic plate. For the filament bilayers considered here, each layer has three local fields that need to be taken into account: the effective layer thickness, which we interpret as being proportional to the spatial density of filaments in that layer; the orthotropic principal growth directions, given by the local tangent and in-plane normal vectors to the filaments; and the orthotropic growth factors in these principal growth directions.

3.1 Density field

To compute the material density field from a discrete set of filaments in a given layer, we interpret density as the distance between the centres of adjacent filaments (h_f) divided by the diameter of each filament (d_f) as shown in Fig. 3. This means the density is always a real number between zero and one with zero being a void and unity corresponding to no gap between filaments. This density will then be used to scale the local thickness field of each layer of the elastic plate.

To compute this density field, we consider as input the parametric description of the print path of each layer, where the centre curve of each filament in the layer is parametrically represented using the Scalable Vector Graphics (SVG) format. This defines each print path as a collection of N_f continuous splines, whose segments are linear, quadratic or cubic Bézier curves. If the parametric equation of the ith filament is $\mathbf{p}_i(t)$, where $\mathbf{p}_i \in \mathbb{R}^2$ and $t \in [0,1]$ is the parametric variable, we can compute the density as a continuous field defined at all $\mathbf{x} \in \mathbb{R}^2$ by convolving each curve in the print path with a smoothing kernel

$$\tilde{\rho}(\mathbf{x}) = \sum_{i=1}^{N_f} \int_0^1 \zeta\left(\mathbf{x} - \mathbf{p}_i(t), \mathbf{p}_i'(t); \sigma\right) \left|\mathbf{p}_i'(t)\right| \mathrm{d}t, \tag{4}$$

where $\zeta(\mathbf{x},\mathbf{y};\sigma)$ is the smoothing kernel and σ is a user-defined scalar parameter that controls the smoothing width (see Fig. 3, left). To define the kernel we choose a tensor product of one-dimensional hat functions oriented along the tangent vector of the filament so that

$$\zeta(\mathbf{x}, \mathbf{y}; \sigma) = \frac{1}{\sigma} w(x^{\parallel}; \sigma) w(x^{\perp}; \sigma), \tag{5}$$

$$x^{\parallel} = |\mathbf{x}\cdot\hat{\mathbf{y}}|, \quad x^{\perp} = |\mathbf{x}\cdot\hat{\mathbf{y}}^{\perp}| \tag{6}$$

$$w(\zeta; \sigma) = \max\left(0, 1 - \frac{|\zeta|}{\sigma}\right), \tag{7}$$

where $\hat{\mathbf{y}}$ is the normalised unit vector along direction $\mathbf{y}$, and $\mathbf{y}^{\perp}$ denotes the transverse vector to $\mathbf{y}$ so that $\mathbf{y}\cdot\mathbf{y}^{\perp} = 0$. This definition makes sure that the density along the centre of an isolated filament is equal to unity, and decays linearly with the distance away from the filament. For an array of parallel straight-line filaments with spacing δ_f, the field is continuously filled whenever $\sigma \geq \delta_f$, in which case the interior field is of average constant value σ/δ_f. If $\sigma \leq \delta_f/2$, zero-density voids appear in the field.

In the rest of this work, we express the parameter σ as a function of the largest filament spacing in any given print path by introducing a non-dimensional parameter η, such that $\sigma = \eta\delta_f^{\max}$. Setting $\eta \geq 1$ ensures that we obtain a density field which is always strictly larger than zero. Wherever the filaments are adjacent, or equivalently if $\delta_f = d_f$ with d_f the filament diameter, the density $\tilde{\rho}$ attains its maximum possible value of σ/d_f. To normalise the density field, we therefore globally rescale the density according to $\rho(\mathbf{x}) = \tilde{\rho}(\mathbf{x})d_f/\sigma$ so that $0 < \rho(\mathbf{x}) \leq 1$. Throughout the rest of this work we set $\eta = 5/4$ as a balance between retaining and smoothing out the features of the print path.

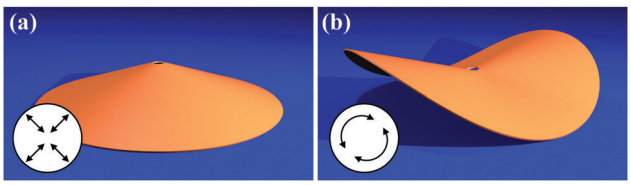

Fig. 2 Examples of homogeneous anisotropic growth of a monolayer disk with $h/R = 0.01$. (a) A radial growth profile with homogeneous 5% growth gives rise to a cone (left). (b) An azimuthal growth profile with the same growth factor leads to a saddle (right).

3.2 Growth directions

In the discrete case, the principal growth directions are defined as being tangent and normal to each filament. To interpolate these directions onto a continuous field, we re-use the density smoothing kernel $\zeta(\mathbf{x},\mathbf{y};\sigma)$ defined above. In particular, with the tangent vector given as $\mathbf{p}'(t)$, we interpolate the growth directions as

$$\mathbf{p}_c(\mathbf{x}) = \sum_{i=1}^{N_f} \int_0^1 \zeta(\mathbf{x} - \mathbf{p}_i(t), \mathbf{p}'_i(t); \sigma)\mathbf{p}'_i(t)\mathrm{d}t, \tag{8}$$

and we finally normalise $\mathbf{p}_c$ to get a unit vector (see Fig. 3, left). We note that the actual growth direction is agnostic to the

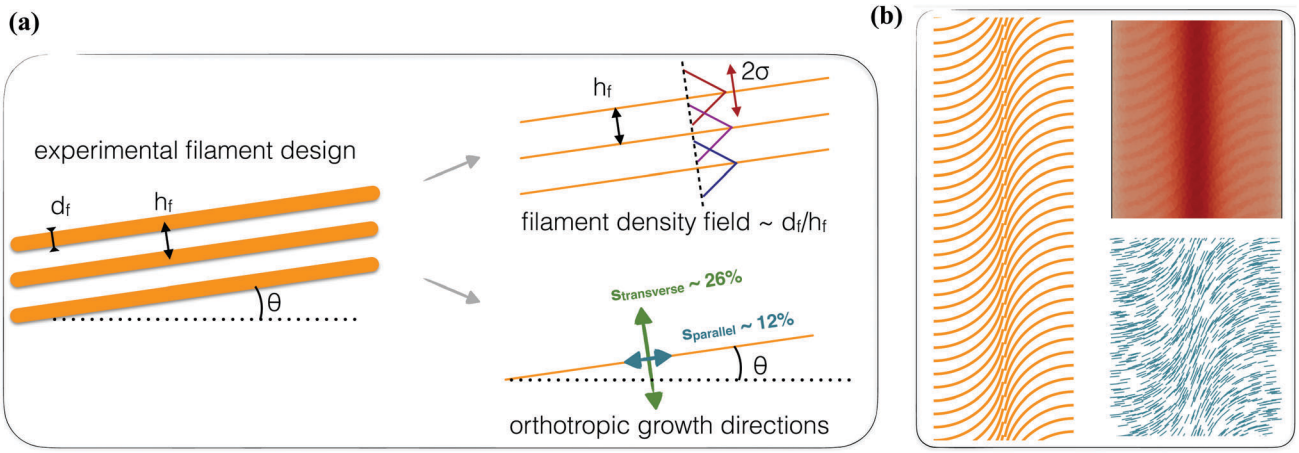

Fig. 3 (a) Schematic illustration of how a discrete filament design with filament diameter d_f, filament spacing h_f, and angle θ (left, in orange), is converted into a continuous filament density field using convolution with a linear kernel (middle, top) and orthotropic growth directions by interpolating the tangent vectors (middle, bottom), as described in (4)–(7). (b) An example of an actually printed filament design (left, in orange), obtained from the bottom layer of the helicoid shape shown below. The figure on the right shows the computed density field (top, red) and directional tangential growth field (bottom, blue) on a segment of the plate computed using $\eta \equiv \sigma/\delta_f = 5/4$.

transformation $\tilde{\mathbf{p}}'_i(t) = -\mathbf{p}'_i(t)$, and so when accumulating the growth directions from different filaments we make sure to orient the tangent vectors of all contributing path segments consistently.

3.3 Growth factors

The growth factors parallel and transverse to the filaments, s_p and s_t respectively, are fixed throughout this work and are chosen based on experimental data ($s_p = 0.12$, $s_t = 0.26$). However, in the experimental results of Gladman *et al.*,[11] it was observed that the bottom layer, or the layer that was printed first, typically swelled more than the top layer. This observation implies that the cross-linking of the material was different between the top and the bottom layers. One hypothesis for this effect is that the polymerisation chemistry in Gladman *et al.*[11] relied on an oxygen scavenger in the catalyst, so that ink that was exposed to oxygen for longer would have experienced more degradation. In the printed bilayer structures, the ink on the bottom layer was quickly shielded from oxygen by the addition of the top layer, whereas the top layer would have been subjected to oxygen for a longer time. As a consequence, the ink constituting the top layer would have had fewer long polymer chains and less entanglement than the ink constituting the bottom layer. Another potential cause for the differential swelling could be that the top layer was exposed to more UV light during baking, causing it to crosslink more than the ink of the bottom layer – though this should have been mitigated by the long baking times adopted in ref. 11. Nevertheless, to account for this observation we introduce a uniform scaling parameter for the growth factors in each of the two layers, denoted μ_1 and μ_2 below.

3.4 Initial conditions

Using the procedure outlined above, we can convert any print path into a continuous density and growth field. We use the density field to set the thickness as $h(\mathbf{x}) = d_f\rho(\mathbf{x})$, so that adjacent filaments correspond to a thickness d_f whereas sparser filament densities have a proportionally smaller thicknesses. We set the Poisson's ratio of the material to $\nu = 0.4$, based on an estimate for hydrogel-type materials.[11]

To compute the growth patterns, we set the rest metric at each point of each layer according to the growth direction (eigenvectors) and growth factors (eigenvalues) defined above:

$$\mathbf{a}_{r1}(\mathbf{x}) = \mathbf{R}_1{}^T(\mathbf{x})\Lambda_1{}^2\mathbf{R}_1(\mathbf{x})$$

$$\mathbf{a}_{r2}(\mathbf{x}) = \mathbf{R}_2{}^T(\mathbf{x})\Lambda_2{}^2\mathbf{R}_2(\mathbf{x})$$

where,

$$\Lambda_l = \mathbf{I} + \mu_l \begin{pmatrix} s_p & 0 \\ 0 & s_t \end{pmatrix}, \quad \mathbf{R}_l(\mathbf{x}) = \begin{pmatrix} \hat{\mathbf{p}}_{c,l}(\mathbf{x}) & \hat{\mathbf{p}}^{\perp}_{c,l}(\mathbf{x}) \end{pmatrix},$$

with $l \in [1,2]$ denoting the bottom and top layer respectively, and μ_l being the respective scaling factors. To show how growth changes the shape of the sheet quasi-statically, we interpolate s_p and s_t from 0 to their final values *via* an arithmetic sequence and compute the embedding that minimises the energy (1), with $\mathbf{a}_r$ and $\mathbf{b}_r$ given by eqn (2), generalised to layers of unequal thickness.[12] This procedure yields a quasi-static path to the global equilibrium.[12,14]

Lastly, to simulate the effect of the transverse swelling on the thickness of the material, we scale the thickness of each layer with the prefactor $(1 + \mu_l s_t)$, so that the thickness increases proportional to the transverse swelling.

4 Comparison with experiments

We start with the computation of four artificial shapes: the helicoid, catenoid, sombrero, and logarithmic spiral, and two natural shapes: a folding flower and an orchid flower. For all shapes, detailed plots of the experimental filament design, and

the numerical initial conditions used, are shown in the ESI.† We summarise the main experimental parameters used for each of the cases in Table 1.

4.1 Helicoid

The helicoid is printed on a rectangular sheet with dimensions $L_x \times L_y$, with L_x = 8 mm the width and L_y = 40 mm the height of the sheet. Each layer has a pattern consisting of circular arcs on each side of the long-axis centreline that each sweep an angle of $\pi/4$, and are anti-symmetric with respect to the y-axis. The top and bottom layers are different, one can be obtained from the other by a rotation of π of the pattern. The spacing between the arcs along the y-direction is 0.75 mm. The experimental structure was printed with a filament diameter of 0.4 mm, and we set μ_1 = 1. A photograph of the experimental result, with a rendering of the numerical solution is shown in Fig. 4, left.

4.2 Catenoid

The catenoid has the same dimensions and design of the helicoid, except that the circular arcs are symmetric with respect to the y-axis, changing their layout from a S-shape for the helicoid to an V-shape for the catenoid. The arc spacing is the same as for the helicoid. For the simulations we use a filament diameter of 0.25 mm and we set μ_1 = 1.025 in order to bias the shape into rolling up, as opposed to ruffling. A photograph of the experimental result, with a rendering of the numerical solution is shown in Fig. 4, middle.

4.3 Logarithmic spiral

The experimental logarithmic spiral is a $0^\circ/90^\circ$ ply printing pattern on a rectangular sheet of dimensions L_x = 64.85 mm and L_y = 5.25 mm. The bottom layer pattern consists of eight parallel straight lines along the x-direction with spacing 0.75 mm. The top layer is a collection of parallel straight lines along the y-direction, with filament spacing increasing according to a power-law with exponent 1.4 when moving towards one end of the spiral. The experimental sample was printed with a filament thickness of d_f = 0.4 mm. The result is a doubly-curved shape, where the principal curvature along the longitudinal axis gradually increases towards one end, so that a logarithmic spiral is formed (Fig. 5, top left).

Running the corresponding numerical simulations, using $\mu_1 = \mu_2 = 1$ and growth factors s_p = 0.12 and s_t = 0.26, we find a less pronounced curvature than the experiments, as shown in Fig. 5, bottom right. To investigate this, we ran a series of simulations gradually changing both the filament thickness, as well as the growth factors. The table in Fig. 5 shows the variations of the resulting shapes.

The smallest value of d_f results in a cylindrical shape rolled-up along the long axis, increasing its winding as the growth factors increase. For the larger values of d_f, a transition occurs: at first, the structure rolls up along the long axis into a cylindrical shape. When the growth factors increase further, though, the curvature in the transverse direction increases, and the resulting doubly-curved shape stiffens like a slap bracelet, causing it to partially unroll again. The best qualitative match with the experimental result is obtained for d_f = 0.4 mm and 60% of the final growth.

4.4 Sombrero

The sombrero is printed on a circular disk with radius R = 7.5 mm. The bottom layer consists of a single spiral filament with radial spacing 0.4 mm. The top layer has a spiral filament, also with radial spacing 0.4 mm, in the inner 3.5 mm radius disk, and a set of radial spokes at the outer part of the disk. The filament diameter of the experimental structure was 0.25 mm, and we set μ_1 = 1.2. A photograph of the experimental result, with a rendering of the numerical solution is shown in Fig. 4, right.

4.5 Folding flower

The printed flower consists of a central disk of radius 2.5 mm, with five petals attached around it. Each petal has a length of 15 mm and has an outline defined by a quadratic curve. The virtual starting point of each petal is offset radially by 1.5 mm with respect to the centre point of the disk. Both bottom and top layers form spirals within the centre disk, with a spiral spacing of 0.4 mm. Each petal consists of a $0^\circ/90^\circ$ ply pattern, where the filaments are spaced by 0.85 mm. The filament diameter of the printed structure was 0.4 mm. For this result, we set μ_1 = 1.2. We ramp up the orthotropic growth factors in each layers from 0 initially to their final values s_p and s_t, and show results at intermediate stages to compare with the temporal evolution of the experiments (Fig. 6).

4.6 Orchid

The printed orchid consists of a disk with six petals attached to it. The two long petals are rectangular strips capped with a circular arc, which are connected to the perimeter of the centre disk at $\pm 58^\circ$ angles with respect to the y-axis. The three short petals have elliptical outlines and are attached to the disk at angles $(-116^\circ, 0^\circ, 116^\circ)$ with respect to the y-axis. Finally, the bottom petal outline is a collection of straight lines and circular arcs. The filament diameter of the experimental structure was 0.325 mm, and we use μ_1 = 1.2. An additional modification we added is to simulate the orchid lying on a flat impenetrable surface, as opposed to all results above which were obtained without any boundary effects. In particular, we pin the centre point of the disk to a horizontal plane aligned with the initial geometry, and add a penalisation term to the total energy that

Table 1 Settings for the different test cases simulated here. The columns represent filament diameter (d_f), non-dimensional smoothing factor (η), and scaling of the growth factor of the bottom (μ_1) and top (μ_2) layers

Case	d_f (mm)	η	μ_1	μ_2
Helicoid	0.40	1.25	1	1
Catenoid	0.25	1.25	1.025	1
Logarithmic spiral	0.40	1.25	1	1
Sombrero	0.25	1.25	1.2	1
Folding flower	0.40	1.25	1.2	1
Orchid	0.325	1.25	1.2	1

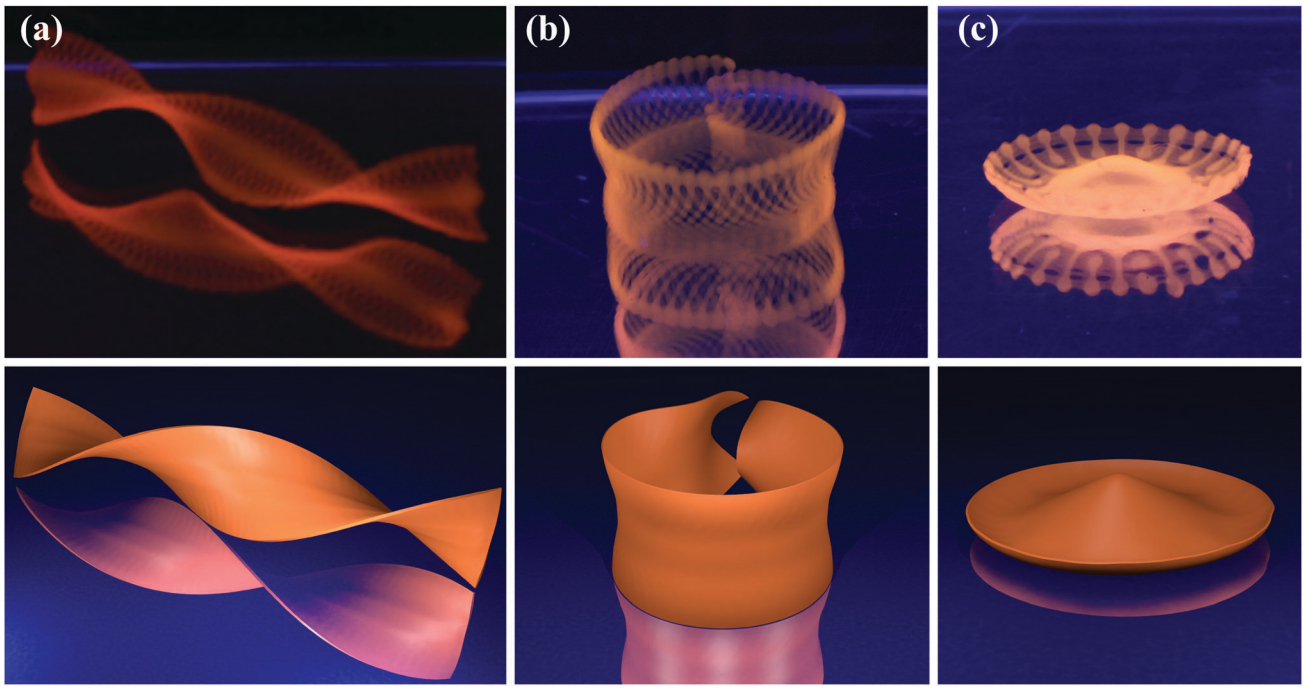

Fig. 4 Experimental and numerical results for (a) the helicoid, (b) the catenoid, and (c) the sombrero. For each shape, experimental photographs are shown on the top, while rendered simulation results are presented on the bottom. The experimental pictures of the helicoid and catenoid are adapted from ref. 11.

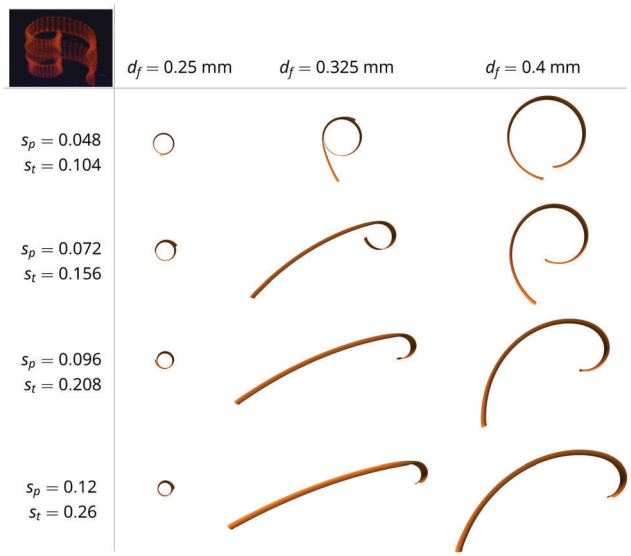

Fig. 5 The numerically computed mid-surface of the swollen shape corresponding to the print path of the logarithmic spiral, for a systematic variation of the filament thickness (horizontally) and growth factors (vertically). The inset on the top left shows the experimental result from ref. 11, which was printed with d_f = 0.4 mm.

penalises any vertex of the mesh crossing that plane. Photographs of the experimental result, with renderings of the numerical solution are shown in Fig. 7. It can be seen that in both cases, the geometry has multiple contact points with the substrate, which justifies our approach to add a surface energy term.

One feature of the experimental sample is a rupture of the top-right long petal from the centre disk. In the simulation, we have access to all stretching strains, and a visualisation of their distribution over the final mid-surface (see ESI†) shows the large strains occurring at the location where the experimental sample ruptured. It is unclear whether the large strains did cause the structural failure in the experiments, as opposed to, for instance, defects in the printed sample. Nevertheless, this analysis shows the additional insights that can be obtained from the numerical results.

5 Discussion

Our approach builds on our knowledge of geometrically nonlinear elasticity of thin shells, discrete differential geometry, and materials engineering to provide a computational approach to calculate the shapes of smooth and printed phytomimetic structures. Continuous sheets can directly be interpreted as elastic plates (or shells) while discrete filament structures can be represented *via* a smoothed representation that allows for variable thickness and orientation of the growth fields. We have shown that this leads to simulated structures that have the same qualitative shapes as their experimental equivalents. Given the experimental variability in printed filament diameters, fibril alignment within each filament, and the lack of precise control over the cross-linking in the hydrogels, closer quantitative comparisons are not viable.

While we focused on connecting our approach to experimental observations with anisotropically swelling inks, our

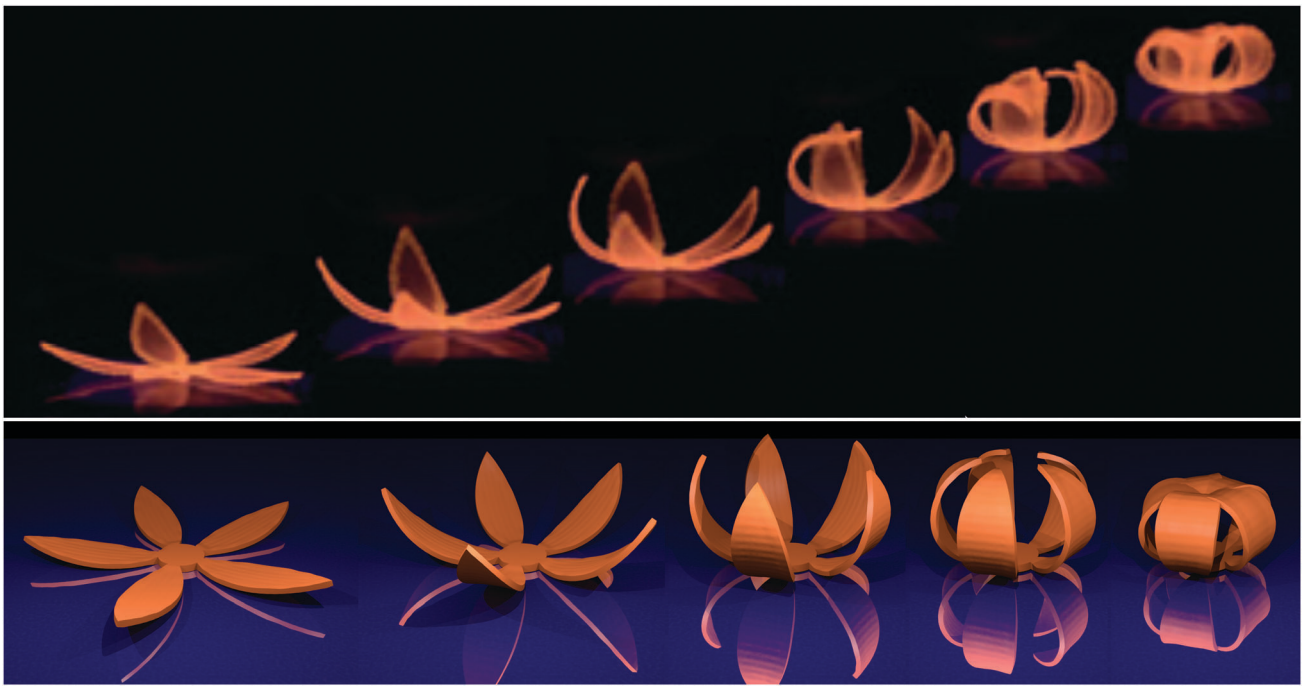

Fig. 6 Experimental and numerical results for the folding flower. Photographs of the experiments are shown above at different temporal stages of the growth process. The bottom pictures show the simulated shapes equilibrated at 5%, 20%, 40%, 60% and 100% of the final growth values. The experimental pictures are adapted from ref. 11.

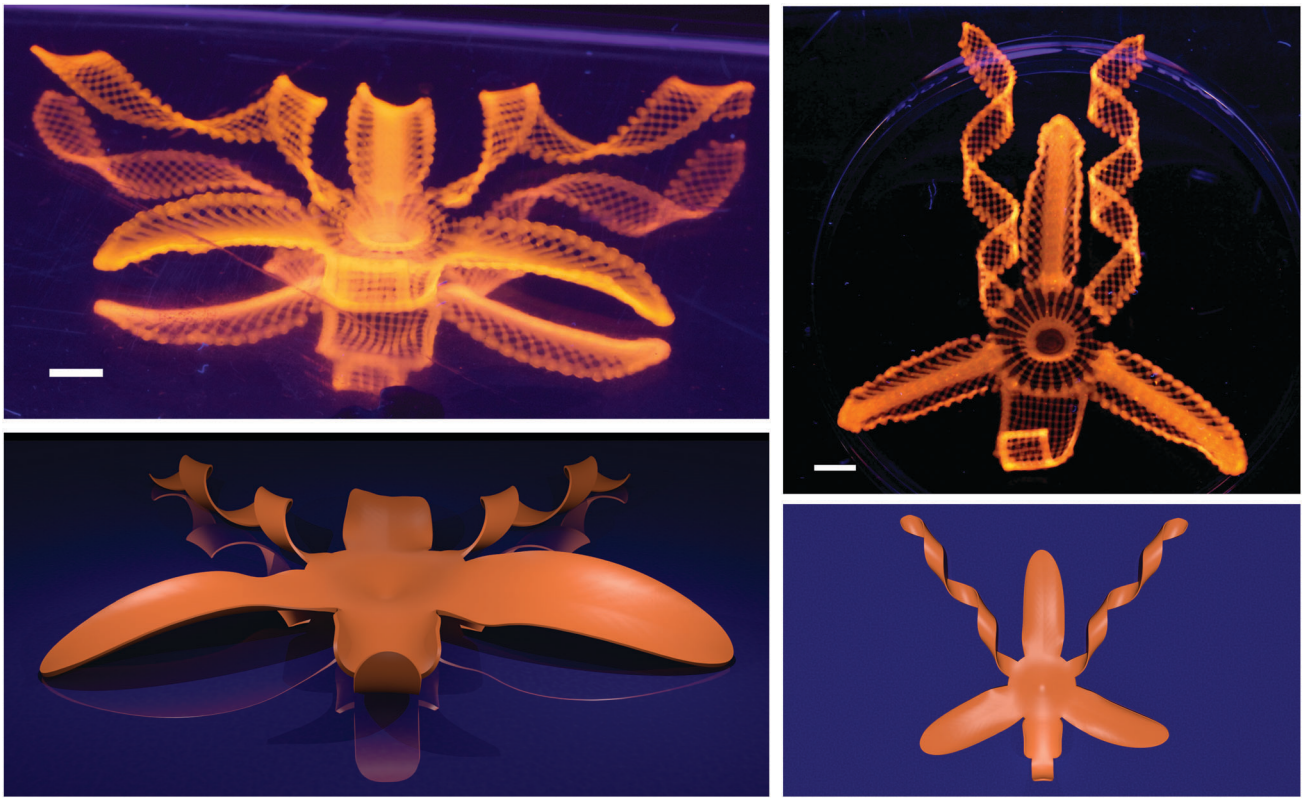

Fig. 7 Experimental and numerical results for the orchid. Photographs of the experiments are above renderings of the simulated shapes. The experimental pictures are adapted from ref. 11.

approach is agnostic to the details of how the changes in the metric tensor and the shape operator are actually implemented. Isotropically growing materials such as hydrogels can be represented by locally scaling the rest metric for each layer, whereas systems like pneumatic elastomers would require a similar orthotropic scaling of the rest metric as performed in this study. We expect that these application-specific models can be built in a relatively straight-forward fashion, and, once calibrated and implemented, simulations as performed here can be a valuable and routine addition to any workflow.

Our numerical results can visualise the sequence of equilibrium growth trajectories between initial and final states, and can thus provide access to the residual stresses and strains within the grown structures, and help systematically investigate the sensitivity of final shapes to initial conditions. When integrating simulations further into the design process, one can further probe the sensitivity of final shapes to external perturbations, investigate energy landscapes corresponding to such changes, and perform simple closed-loop optimisation algorithms to iterate on the inverse-design problem. These features ought to be useful for more systematic theoretical and numerical studies of the rapidly developing field of elastic shape-shifting mono- and bilayer structures.

Conflicts of interest

There are no conflicts to declare.

Acknowledgements

We thank the Swiss National Science Foundation for support (P2EZP2_159091, P300P2_171419) through a postdoctoral grant (WMvR), the American Bureau of Shipping for support through a Career Development Chair at MIT (WMvR), and the National Science Foundation for support from DMR 14-20570 and DMR 15-33985 (JAL, LM). The software used in this manuscript has been released under the BSD 3-Clause open-source license and can be downloaded from https://github.com/wimvanrees/growth_SM2018.

References

1 D. Chen, J. Yoon, D. Chandra, A. J. Crosby and R. C. Hayward, *J. Polym. Sci., Part B: Polym. Phys.*, 2014, **52**, 1441–1461.
2 R. L. Truby and J. A. Lewis, *Nature*, 2016, **540**, 371–378.
3 T. van Manen, S. Janbaz and A. A. Zadpoor, *Mater. Today*, 2017, **21**, 144–163.
4 S. Tibbits, *Arch. Design*, 2014, **84**, 116–121.
5 Q. Ge, H. J. Qi and M. L. Dunn, *Appl. Phys. Lett.*, 2013, **103**, 131901.
6 R. Fernandes and D. H. Gracias, *Adv. Drug Delivery Rev.*, 2012, **64**, 1579–1589.
7 S. Felton, M. Tolley, E. Demaine, D. Rus and R. J. Wood, *Science*, 2014, **345**, 644–646.
8 M. Wehner, R. L. Truby, D. J. Fitzgerald, B. Mosadegh, G. M. Whitesides, J. A. Lewis and R. J. Wood, *Nature*, 2016, **536**, 451–455.
9 Y. Klein, E. Efrati and E. Sharon, *Science*, 2007, **315**, 1116–1120.
10 J. Kim, J. A. Hanna, M. Byun, C. D. Santangelo and R. C. Hayward, *Science*, 2012, **335**, 1201–1205.
11 A. S. Gladman, E. A. Matsumoto, R. G. Nuzzo, L. Mahadevan and J. A. Lewis, *Nat. Mater.*, 2016, **15**, 413–418.
12 W. M. van Rees, E. Vouga and L. Mahadevan, *Proc. Natl. Acad. Sci. U. S. A.*, 2017, **114**, 11597–11602.
13 M. B. Amar and A. Goriely, *J. Mech. Phys. Solids*, 2005, **53**, 2284–2319.
14 M. Marder and N. Papanicolaou, *J. Stat. Phys.*, 2006, **125**, 1065–1092.
15 J. Dervaux and M. B. Amar, *Phys. Rev. Lett.*, 2008, **101**, 068101.
16 E. Efrati, E. Sharon and R. Kupferman, *J. Mech. Phys. Solids*, 2009, **57**, 762–775.
17 H. Liang and L. Mahadevan, *Proc. Natl. Acad. Sci.*, 2009, **106**, 22049–22054.
18 M. Lewicka, L. Mahadevan and M. R. Pakzad, *Proc. R. Soc. A*, 2011, **467**, 402–426.
19 D. J. Struik, *Lectures on Classical Differential Geometry*, Dover Publications, 2nd edn, 1988.
20 C. Weischedel, A. Tuganov, T. Hermansson, J. Linn and M. Wardetzky, Construction of discrete shell models by geometric finite differences, Fraunhofer ITWM Technical Report 220, 2012.
21 J. N. Reddy, *Mechanics of Laminated Composite Plates and Shells*, CRC Press, 2nd edn, 2004.
22 E. Grinspun, Y. Gingold, J. Reisman and D. Zorin, *Comput. Graph. Forum*, 2006, **25**, 547–556.
23 D. C. Liu and J. Nocedal, *Math. Prog.*, 1989, **45**, 503–528.
24 R. Tamstorf and E. Grinspun, *Graph. Models*, 2013, **75**, 362–370.
25 G. Guennebaud and B. Jacob, *et al.*, *Eigen v3*, 2010, http://eigen.tuxfamily.org.
26 A. Jacobson and D. Panozzo, *et al.*, *libigl: a simple C++ geometry processing library*, 2016, http://libigl.github.io/libigl/.
27 J. Reinders, *Intel Threading Building Blocks: outfitting C++ for multi-core processing parallelism*, O'Reilly Media, Inc, USA, 2007.
28 J. R. Shewchuk, in *Applied Computational Geometry Towards Geometric Engineering*, Springer Nature, 1996, pp. 203–222.
29 C. D. Modes, K. Bhattacharya and M. Warner, *Proc. R. Soc. A*, 2010, **467**, 1121–1140.